

## RESEARCH LETTER

10.1002/2015GL066246

## Key Points:

- Thermal control inconsistent with anisotropy structure and interfaces in the uppermost mantle
- Hypothesis tests imply that pure LPO is not an ideal model for radially anisotropic structure
- SPO due to partial melting or petrological fabrics better explain observations

## Supporting Information:

- Text S1, Figures S1–S9, and Tables S1–S3
- Figure S1
- Figure S2
- Figure S3
- Figure S4
- Figure S5
- Figure S6
- Figure S7
- Figure S8
- Figure S9

## Correspondence to:

L. Auer,  
ludwig.auer@tomo.ig.erdw.ethz.ch

## Citation:

Auer, L., T. W. Becker, L. Boschi, and N. Schmerr (2015), Thermal structure, radial anisotropy, and dynamics of oceanic boundary layers, *Geophys. Res. Lett.*, *42*, 9740–9749, doi:10.1002/2015GL066246.

Received 22 SEP 2015

Accepted 28 OCT 2015

Accepted article online 2 NOV 2015

Published online 19 NOV 2015

## Thermal structure, radial anisotropy, and dynamics of oceanic boundary layers

Ludwig Auer<sup>1</sup>, Thorsten W. Becker<sup>2</sup>, Lapo Boschi<sup>3,4</sup>, and Nicholas Schmerr<sup>5</sup>

<sup>1</sup>Institut für Geophysik, Eidgenössische Technische Hochschule Zürich, Zürich, Switzerland, <sup>2</sup>Department of Earth Sciences, University of Southern California, Los Angeles, California, USA, <sup>3</sup>UMR 7193, Institut des Sciences de la Terre Paris, Sorbonne Universités, UPMC Univ Paris 06, Paris, France, <sup>4</sup>CNRS, UMR 7193, Institut des Sciences de la Terre Paris (ISTeP), Paris, France, <sup>5</sup>Department of Geology, University of Maryland, College Park, Maryland, USA

**Abstract** Defining the oceanic lithosphere as a thermal boundary layer allows to explain, to first order, age-dependent bathymetry and isotropic wave speeds. In contrast, SS precursors and receiver functions suggest a subhorizontal interface within this layer, on top of a radially anisotropic zone. Comparing a suite of geodynamic scenarios against surface wave dispersion data and seismic discontinuities, we find that only weak age dependency of the radially anisotropic zone is compatible with observations. We show that this zone is confined from below by a second weaker seismic interface. While observed azimuthal anisotropy is consistent with lattice-preferred orientation of olivine due to asthenospheric flow underneath the lithosphere, radial anisotropy requires additional contributions, perhaps from petrological fabrics or melt ponding. This implies that seismic reflectors previously associated with the base of the lithosphere are instead associated with preserved structures embedded in it. They carry information about plate formation but have little control on plate deformation.

### 1. Introduction

To first order, the oceanic lithosphere can be understood as the upper thermal boundary layer of mantle convection that forms at the mid-ocean spreading centers and grows thicker as the plate is carried away, thus having more time to cool down to larger depths. The underlying asthenosphere is warmer, hence, more ductile and separated by a rheological transition region from the mechanically stronger lithosphere. This thermomechanical definition of the lithosphere is partially supported by bathymetry [e.g., *Zhong et al.*, 2007], depth dependence of seismicity [e.g., *Chen and Molnar*, 1983; *McKenzie et al.*, 2005], effective elastic thickness variations [e.g., *Watts et al.*, 2013], and isotropic shear velocity ( $v_S$ ) structure which largely conform to half-space cooling (HSC) [e.g., *Ritzwoller et al.*, 2004].

The thermal influence on upper mantle structure can be visualized by referencing tomographic shear velocity models against seafloor ages [e.g., *Zhang and Tanimoto*, 1991; *Priestley and McKenzie*, 2013]. Such analysis, based on the isotropic component of the global model *savani* [Auer et al., 2014] and ages from Müller et al. [2008] (Figure 1) is, to first order, consistent with HSC estimates, as illustrated, for example, in Figures 1a and 1b, where wave speeds underneath the Pacific and the Atlantic oceans are compared against HSC isotherms.

Upper mantle seismic anisotropy, which can also be imaged through tomography, provides further constraints on boundary layer dynamics [e.g., *Long and Becker*, 2010]. Two forms of anisotropy are typically considered: (i) radial anisotropy, i.e., the velocity ratio of horizontally traveling, horizontally polarized shear waves,  $v_{SH}$ , and horizontally traveling, vertically polarized shear waves,  $v_{SV}$ , (quantified as  $\xi = v_{SH}^2/v_{SV}^2$ ), and (ii) azimuthal anisotropy, i.e., the dependence of Love and Rayleigh wave velocities, at a given location, on the orientation of propagation. Azimuthal anisotropy is present in the oceanic lithosphere and uppermost asthenosphere [e.g., *Montagner and Tanimoto*, 1991; *Plomerová et al.*, 2002; *Maggi et al.*, 2006; *Ekström*, 2011; *Burgos et al.*, 2014]. Alignment of fast axes with the inferred shear from absolute plate motion models is oceanic basin dependent [e.g., *Debayle and Ricard*, 2013; *Beghein et al.*, 2014], but when lattice-preferred orientation (LPO) of olivine is inferred from mantle flow models, the global match underneath plates is found to be uniformly good [Becker et al., 2014].

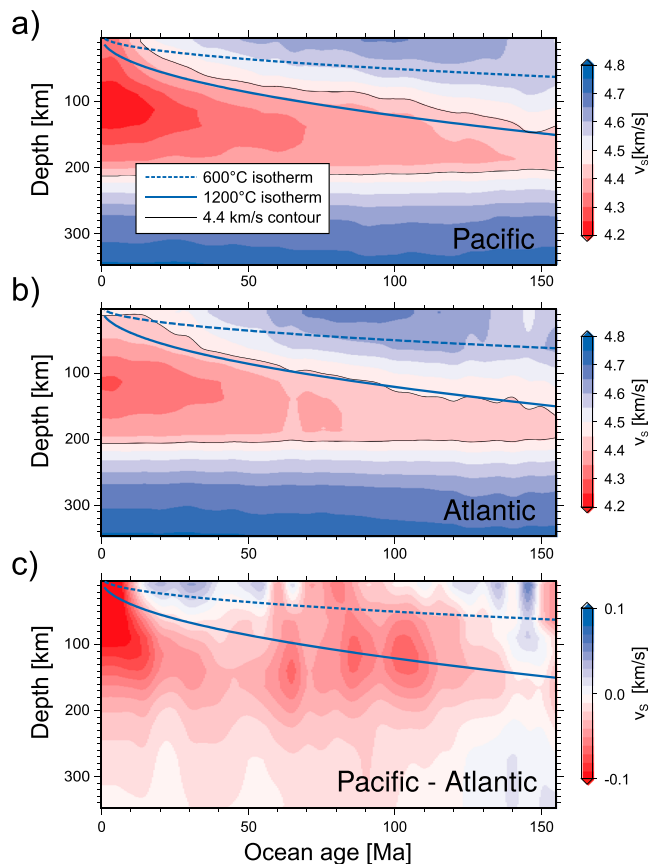


**Figure 1.** Isotropic velocities derived from the anisotropic tomography *savani* [Auer *et al.*, 2014], referenced against seafloor age from Müller *et al.* [2008]. To first order, (a) the Pacific and (b) the Atlantic oceans are broadly consistent with half-space cooling: The 1200°C isotherm loosely follows the 4.4 km/s isoline and confines an underlying low-velocity zone. An asthenospheric temperature of 1315°C and temperature-dependent conductivity [cf. McKenzie *et al.*, 2005] was used. Employed regionalization polygons are shown in Figure S1 in the supporting information. (c) Atlantic signal subtracted from the Pacific.

Upper mantle radial anisotropy is most pronounced underneath the Central Pacific and generally described as a 80–100 km thick layer of increased  $\xi$  [e.g., Ekström and Dziewonski, 1998; Boschi and Ekström, 2002; French *et al.*, 2013; Burgos *et al.*, 2014; Beghein *et al.*, 2014; Auer *et al.*, 2014; Moulik and Ekström, 2014] peaking at 100–120 km depth. The anomaly appears spatially uncorrelated with patterns of azimuthal anisotropy [e.g., Becker *et al.*, 2014], and its upper bound is significantly flatter than what HSC-related structure would imply, as shown for the model *savani* in Figure 2 (top left). This is consistent with recent work by Burgos *et al.* [2014] and Beghein *et al.* [2014]. Yet earlier studies had reported weak age dependency of the radially anisotropic layer [Nettles and Dziewoński, 2008; Kustowski *et al.*, 2008].

Body wave receiver functions [e.g., Rychert and Shearer, 2009; Kawakatsu *et al.*, 2009; Kumar and Kawakatsu, 2011] and short- and long-period SS precursors [e.g., Rychert and Shearer, 2011; Schmerr, 2012] provide further constraints to structure and discontinuities in the upper mantle. Often, these data sets indicate a sharp negative velocity contrast underneath the oceans at an average depth of  $\sim 60$  km [Revenaugh and Jordan, 1991; Kumar and Kawakatsu, 2011; Schmerr, 2012], which is often termed the oceanic Gutenberg discontinuity, or *G* [cf. Gutenberg, 1926]. The Rychert and Shearer [2009] and Kumar and Kawakatsu [2011] receiver function estimates of *G* depth are only weakly dependent on seafloor age. Schmerr [2012] also notes subtle age dependency much weaker than expected from a purely thermally controlled lithospheric thickness. In contrast, Rychert and Shearer [2011] found age-dependent depth variations between 25 and 130 km for their long-period SS-based interfaces.

Superimposing the interface estimates of Schmerr [2012] and Kumar and Kawakatsu [2011] upon the  $\xi$  component of *savani* (Figure 2, top left), the similarity between the upper boundary of the high- $\xi$  zone and the

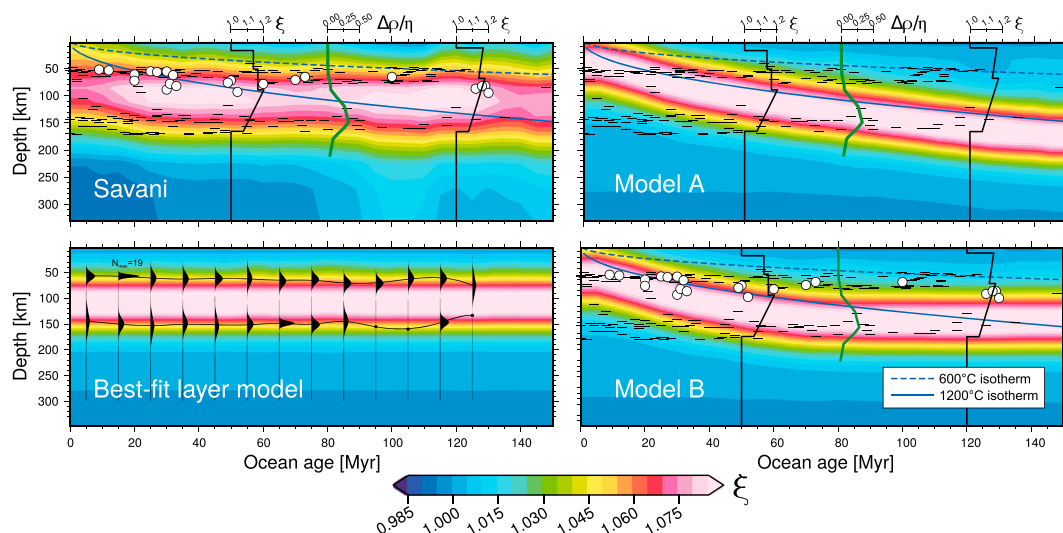


**Figure 2.** (top left) Radial anisotropy underneath the Pacific from *savani* [Auer et al., 2014],  $\xi = (v_{SH}/v_{SV})^2$ , referenced against Pacific seafloor ages [Müller et al., 2008]. The high- $\xi$  zone is nearly independent of age [Burgos et al., 2014; Beghein et al., 2014], its top coincides with the receiver function estimate of the Gutenberg discontinuity [Kumar and Kawakatsu, 2011] (white dots), and its top and bottom coincide with discontinuities from SS precursors [Schmerr, 2012] (black strokes). The left and right thick black lines show the models PA5 and PHB3 of Gaherty et al. [1996] and Gaherty et al. [1999], respectively. The anisotropy depth bracket matches a peak in melt mobility [Sakamaki et al., 2013] (green line, indicating density anomaly,  $\Delta\rho$ , divided by viscosity,  $\eta$ , from a simple thermal model). (bottom left) Best fit layer model for the Pacific; interface depths from SS precursors are represented via black histograms (see text). (right) Selected (top) strongly (Model A) and (bottom) weakly (Model B) age-dependent hypotheses.

Gutenberg discontinuity ( $\sim 60$  km) becomes apparent [Beghein et al., 2014]. Based on the complete data set of Schmerr [2012], we also identify a similar (albeit weaker), deeper interface to approximately coincide with the lower bound of the high- $\xi$  zone at a depth of  $\sim 150$  km. While the shallower G discontinuity is relatively well described [e.g., Rychert and Shearer, 2011; Rychert et al., 2012; Kumar and Kawakatsu, 2011; Schmerr, 2012], there are fewer observations of the deeper interface. Gaherty et al. [1996, 1999] incorporate an interface at comparable depth in their regional 1-D models PA5 and PHB3 (defined along Pacific age corridors of  $\sim 50$  Ma and  $\sim 120$  Ma, respectively; black lines in Figure 2) and identify it with the oceanic manifestation of the Lehmann discontinuity, which is well described for continental regions (with an average depth of  $\sim 220$  km). The deeper interface in the data set of Schmerr [2012] appears laterally less continuous than the G, is mostly associated with spreading centers or hot spots, and modeled as a set of negative velocity contrasts (i.e., a drop in  $v_s$  with depth) or a single positive velocity increase.

In summary, it appears that different seismological observations point to different inferences on lithospheric structures and their relation to temperature, leading to the question of whether the bulk of the observed radial anisotropy is a direct consequence of plate-induced shearing, whether there is significant contribution from other mechanisms [Karato, 2012; Beghein et al., 2014; Burgos et al., 2014; Becker et al., 2014], or whether there are simply shortcomings in resolution or other issues that prevent a correct interpretation. For example, some authors have suggested trade-offs with poorly modeled crustal structure as a potential issue in imaging anisotropic structure [e.g., Ferreira et al., 2010] while our own comparisons between tomographies using CRUST2.0 [Bassin et al., 2000] and its high-resolution successor CRUST1.0 [Laske et al., 2013] have not shown dramatic changes in the recovered anisotropy patterns [Auer et al., 2014].

Tomographic inversions for  $\xi$  may also suffer from subjective parameterization and regularization choices. For instance, regularization schemes that “smooth” tomographic images might, depending on a model’s vertical and horizontal resolution, mask the signature of lithospheric age and favor age-independent models. We explore these issues by conducting forward calculations for conceptual shear velocity models that are based both on geodynamics and tomography and measuring the fit to seismic data. Finally, we reconcile our new results with additional seismological and mineralogical constraints with the ultimate goal of identifying a unified model of the oceanic uppermost mantle.

## 2. Geodynamic Hypothesis Tests

### 2.1. Method and Data

Our experiments follow the probabilistic approach advocated by *Tarantola* [2006] and are based on the idea that rather than inverting data to derive one best solution, it is preferable to construct models based on geologically founded intuition and prior knowledge and falsify them against data, to pass from an a priori to a posteriori collection of admissible solutions. Our geodynamic-seismological hypotheses are designed to reflect robust features of tomography as well as the a priori structure one expects from fundamental geodynamic considerations. Given that  $v_s$  structure is resolved much better than anisotropy [e.g., *Becker et al.*, 2008; *Auer et al.*, 2014], the isotropic component of all forward tests is fixed to a new 3-D background model, based on path-averaged Love and Rayleigh phase velocity data sets up to the sixth overtone and measured at periods between 25 and 300 s from *Visser et al.* [2008] and *Ekström* [2011]. See Table S3 in the supporting information (SI) for a complete overview of the employed data sets. The new model is optimized for high vertical resolution, covers the upper 400 km of the mantle, and is hereafter referred to as *savanUM*. *SavanUM* is largely consistent with its whole-mantle counterpart *savani* but shows higher  $\xi$  amplitudes and a steeper gradient at the top of the anisotropic layer (Figures 2, S2, and S3). For our global surface wave data set *savanUM* achieves a 0.85 variance reduction (VR), defined here as

$$VR = 1 - \frac{|\mathbf{A} \cdot \mathbf{x} - \mathbf{d}_{\text{obs}}|}{|\mathbf{d}_{\text{obs}}|} \quad (1)$$

which can be compared to the data fit of models considered in our hypothesis tests. In equation (1), the linear system matrix  $\mathbf{A}$  comprises the sensitivity functions, relating the model vector  $\mathbf{x}$  to entries of the data vector  $\mathbf{d}_{\text{obs}}$ . Surface wave sensitivity kernels are computed in a ray-theoretical framework, where rays are approximated via the great-circle paths between sources and receivers [see *Auer et al.*, 2014, Figure 1a], for local crustal profiles from CRUST2.0 on top of 1-D PREM [*Dziewoński and Anderson*, 1981] to set up a linear tomography system  $\mathbf{A} \cdot \mathbf{x} = \mathbf{d}_{\text{obs}}$ . Instead of solving this linear system in an inverse sense, our hypothesis tests entail computing synthetic data for different geodynamic model hypotheses, via the dot product between  $\mathbf{A}$  and the “synthetic” model  $\mathbf{x}_{\text{syn}}$ . Thus, different values for the parameters (summarized in Table S2) controlling  $\xi$  in  $\mathbf{x}_{\text{syn}}$  can be explored while monitoring the associated model variance reduction (equation (1)).

We construct a series of geodynamic model hypotheses in terms of  $\xi$  and  $\delta v_s = \frac{\Delta v_s}{v_s}$  on a  $1^\circ \times 1^\circ$  regular grid and then change to a tomographic parameterization, by converting to  $\delta v_{SV}$  and  $\delta v_{SH}$  and projecting onto a coarser equal-area ( $5^\circ \times 5^\circ$  at the equator) voxel mesh having 70 layers with a thickness of 5 km each. Continental radial anisotropy in the geodynamic forward hypothesis tests is prescribed to the layer average of *savanUM*'s continental  $\xi$  to focus on the effect of oceanic structure alone. Radial anisotropy underneath oceans is restricted to vary by only a few geodynamically motivated parameters.

To perform the forward modeling tests, we repartition the global surface wave data set introduced above into three subsets for the Pacific, the Indian, and the Atlantic oceans, by extracting great-circle paths that are exclusively spanning the different oceanic regions and are recorded at stations close to the coast, so that influence from continental regions is minimized.

### 2.2. Age-Independent Geodynamic Hypotheses

We first consider the hypothesis that the anisotropic zone extends across the entire suboceanic asthenosphere and is completely independent of seafloor age. Vertically,  $\xi(z)$  is prescribed to follow a Gaussian, defined here as

$$\xi(z) = \xi_{\text{max}} \exp\left(-\frac{(z - z_0)^2}{2\sigma^2}\right) \quad (2)$$

encapsulating an anisotropy amplitude factor  $\xi_{\text{max}}$ , the depth  $z$ , an offset depth  $z_0$ , and the standard deviation  $\sigma = h/\sqrt{2 \ln 2}$ . The full width at half maximum  $h$  is then in practice controlling the zone's thickness. We first fix  $h$  at 90 km and perform a grid search over the peak amplitude  $\xi_{\text{max}}$ , varied in increments of 0.005 between 1 and 1.2, and the layer offset depth  $z_0$ , varied between 0 and 230 km in 5 km steps.

Monitoring the VR for each hypothesis (Figure 3a) allows to identify, to first order, an optimal set of  $\xi_{\text{max}}$ - and  $z_0$  values for each oceanic basin. Our results confirm that radial anisotropy is essential to jointly fit Love and Rayleigh wave data (as shown by the decreasing data fit for  $\xi_{\text{max}} \rightarrow 1.0$ ) and show that best fit values for depth and strength of anisotropy can be roughly identified. We define informal error margins according

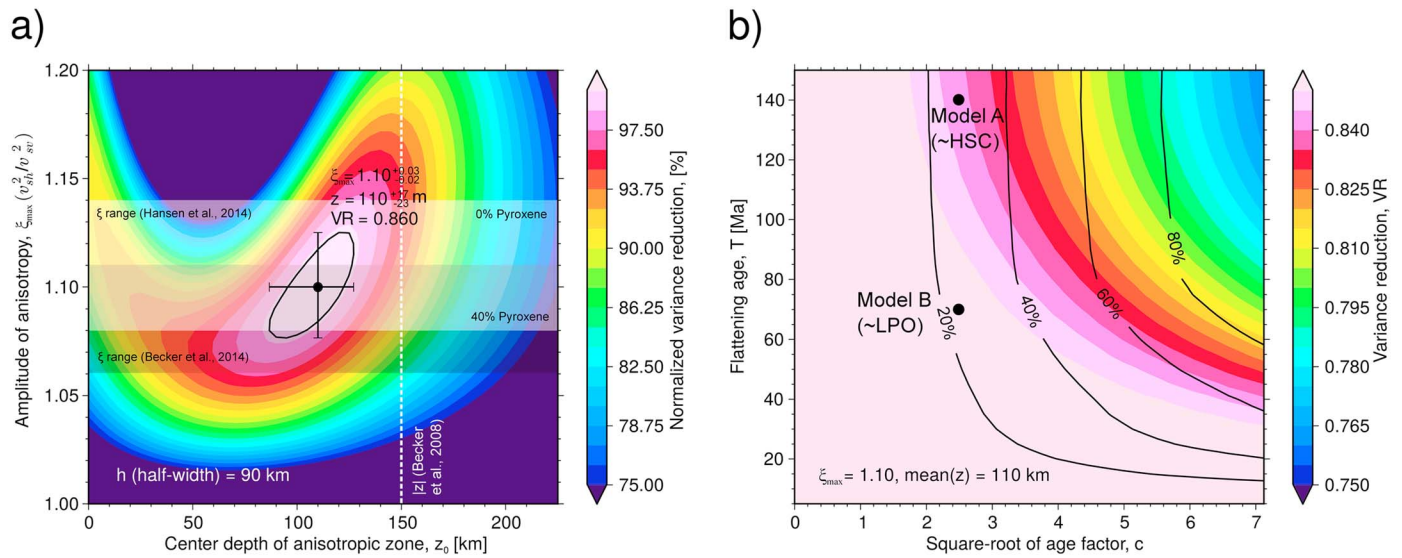


**Figure 3.** (a) Variance reductions for the Pacific data, illuminating depth-versus-anisotropy strength tradeoffs and best fit parameter ranges when the anisotropic layer is approximated with an age-independent Gaussian. The dark and white zones represent geodynamic and experimental LPO predictions of peak radial anisotropy strength, from *Becker et al.* [2008] (Figure S6) and *Hansen et al.* [2014], respectively, for regular A-type fabrics, and the white dashed line shows average peak depth from *Becker et al.* [2008]. (b) Variance reductions in the case where we vary between age-dependent and flat-layer-type conceptual models. There is some preference for entirely age-independent models and models that flatten out at young ages (e.g., model B) over models that follow geodynamically meaningful isotherms (like the 1200°C isotherm; model A). Black isocontours mark the normalized roughness associated with each model and show that age-independent models are smoothest.

to an insignificant 1% change in normalized variance reduction  $VR' = (VR - VR_{\min}) / (VR_{\max} - VR_{\min}) \cdot 100$ , where  $VR_{\min}$  and  $VR_{\max}$  are the minimum and maximum values of VR, respectively. Different oceanic basins are characterized by similarly shaped misfit contours but yield different best fit values for  $\xi_{\max}$  and  $z$ . The Pacific data set requires a stronger and deeper anisotropic anomaly compared to the Indian and Atlantic, with  $z_0$  of  $\approx 110$  km and 80 km and  $\xi_{\max}$  of 1.1 and 1.07 for Pacific and Atlantic, respectively (Table S1). This suggests intraoceanic differences, perhaps related to different spreading rates, consistent with the geodynamic estimates of *Becker et al.* [2008] (Figure S6). Repeating the experiments described above with a boxcar function instead of a Gaussian to approximate the anisotropic zone yields very similar overall trends (see Figures S7 and S8).

Figure 3a compares the flat anisotropy layer depth and strength for the Pacific with approximate estimates of  $\xi$  from dry, “A”-type [Karato et al., 2008] LPO experiments of *Hansen et al.* [2014] (from full saturation as of their Figure 7) for a range of pyroxene contents, and the synthetic LPO models for 30% enstatite [Becker et al., 2006] of *Becker et al.* [2008]. Assuming perfect horizontal alignment, the laboratory LPO estimates are broadly compatible with imaged  $\xi$  amplitudes for realistic pyroxene fractions.

Having identified a set of best fit offset depths and the anisotropy peak amplitudes, we perform an additional two-dimensional grid search, this time over thickness  $h$  and anisotropy strength  $\xi_{\max}$ , with a fixed center depth, to assess trade-offs between those two parameters. As shown in Figure S5, the VR surface less clearly plateaus at a certain best fit set of parameters, which shows that thickness and anisotropy amplitude significantly trade-off with each other, manifesting in a rather broad zone of different combinations of  $\xi_{\max}$  peak amplitudes and thicknesses  $h$  (corresponding to similar total anisotropy “strength,”  $h \cdot \xi_{\max}$ ) that achieve almost the same data misfits. While, for convenience, we present “best fit” layer models for the different oceans, our results will depend on assumptions such as isotropic structure and theoretical simplifications. Hence, relative variations of best fit parameters are more meaningful than absolute values.

We next compare the best fit layer model depth and thickness for the Pacific Ocean with the body wave interface estimates from *Schmerr* [2012] in Figure 2 (bottom left). Instead of plotting the raw depth measurements, we bin the lower and the upper depths in bins of 10 Ma and represent the data in each bin via Gaussians. Where too few measurements are available, a dot marker is plotted at the mean depth instead. Through the mean depths we fit a spline function, facilitating a visual comparison of the model and the SS precursor depths.

With the exception of a region at  $\sim 110$  Ma, the match between both top and bottom reflections and the flat layer radial anisotropy model is good.

### 2.3. Age-Dependent Geodynamic Hypotheses

We next test whether age-dependent versus age-independent models can be discriminated by our regionalized data sets. To this end, we construct models that follow the HSC solution

$$T' = \frac{T - T_0}{T_1 - T_0} = \operatorname{erf}\left(\frac{z}{2\sqrt{\kappa\tau}}\right), \quad (3)$$

where  $T_0$  is surface temperature,  $T_1$  asthenospheric temperature,  $T$  temperature,  $\tau$  age, and  $\kappa$  thermal diffusivity [Turcotte and Schubert, 2002]. Evaluating this equation for explicit choices of  $T'$ , one obtains the lithospheric thickness

$$z_L = c\sqrt{\kappa\tau}, \quad (4)$$

where  $c = 2 \cdot \operatorname{erf}^{-1}(T')$ . In the case of an isotherm for a mantle temperature  $T_1$  of  $1315^\circ\text{C}$ , a surface temperature  $T_0$  of  $14^\circ\text{C}$ , and a constant  $\kappa$  of  $10^{-6} \text{ m}^2/\text{s}$ ,  $c$  would take a value of  $\sim 2.5$ . An age-dependent model of  $\xi$  is constructed via equation (2) as above, but setting the offset depth to

$$z_1 = a + c\sqrt{\kappa\hat{\tau}(\mathbf{x}, f)} \quad (5)$$

at location  $\mathbf{x}$ , where equation (5) approximates models that flatten out after a certain age:  $c$  still controls the slope of the thickness curve and  $a$  defines the Gaussian's offset depth at the spreading center.  $a$  is chosen such that  $z_1$ , averaged over the oceanic basin under investigation, is equal to the best fit depth of the flat-layer case from Figure 3a. The function  $\hat{\tau}$  is given by

$$\hat{\tau}(\mathbf{x}, f) = \begin{cases} \tau(\mathbf{x}) & \text{for } \tau(\mathbf{x}) < f \\ f & \text{for } \tau(\mathbf{x}) \geq f \end{cases} \quad (6)$$

where  $\tau(\mathbf{x})$  are the ages from Müller *et al.* [2008]. We vary between age-independent end-member  $\xi$  models (i.e., the flat layer cases, with the age factor  $c \rightarrow 0$  or the flattening age  $f \rightarrow 0$ ) and age-dependent models following different HSC isotherms and turning flat at larger ages.

We again perform a two-dimensional grid search, now over  $c$  and  $f$ , keeping  $h$  at 90 km and  $z_0$  fixed at the best fit value found for the flat layer case. We vary  $c$  in a relevant range from zero to  $\sim 7$ . Figure 3b for the Pacific shows that for a fixed average depth of 110 km, misfits generally increase when transforming from flat ( $c = 0$ ) to different age slopes ( $c \rightarrow 7$ ). For the global data set, misfits show the same behavior, qualitatively. For young flattening ages  $f < 40$ , however, there is no significant increase in misfit for higher values of  $c$ , delineating a range of weakly age-dependent models which explain the data equally well.

We illustrate the results via two particulars (Figure 3b), model B with a HSC type of age dependence but flattening at  $f = 70$  Ma and model A with the full age dependence one would expect from the  $1200^\circ\text{C}$  HSC isotherm [cf. Becker *et al.*, 2014]. As indicated by their position in the misfit contour map, model A fits the data worse, confirming that strong age dependence is not an ideal model for the  $\xi$  anomaly. The "roughness" of our conceptual models (black contours in Figure 3b) reflects their lateral and vertical continuity and shows that age-independent model scenarios are systematically smoother, as anticipated. Notice that tomographic inversions regularized via roughness damping naturally result in smoother models and are therefore biased toward age-independent models.

To evaluate how much these results depend on the chosen a priori depth, we rerun the Pacific example choosing  $z_0$  to be 20 km below and above the best fit layer depth (see Figure S9). The tests confirm the general age-dependency trends and show that misfits for both offset cases are slightly lower, again suggesting an optimal depth range for the anisotropic region.

## 3. Discussion

Comparisons between the seismological models of  $\xi$  and the data set of Schmerr [2012] show that not only the top of the anisotropic zone correlates with SS precursor depths (as already pointed out by Beghein *et al.* [2014]) but that also the bottom of the zone shows a similar correlation with a deeper impedance contrast (Figure 2),

bracketing radial anisotropy from below. Previously, the shallower of the two interfaces ( $G$ ) had been associated with the bottom of the lithosphere [Rychert and Shearer, 2011]. Such an interpretation questions the geodynamic paradigm of a mainly age- and HSC-controlled lithosphere, which would predict a diffuse and strongly age-dependent lithosphere-asthenosphere transition. Given the results from azimuthal anisotropy that are consistent with a mechanical lithosphere being controlled by HSC, the shallow impedance contrast seems to be better described as a midlithospheric discontinuity (MLD) similar to a boundary widely reported for the continents [e.g., Selway et al., 2015].

### 3.1. Structural Complexity Beyond Half-Space Cooling

The seismic interfaces and the radially anisotropic layer are, of course, not the only features displaying thermal boundary layer complexities that require an interpretation beyond HSC. Even isotropic wave speeds that should theoretically be more directly linked to temperature distribution show regional deviations from the simple global HSC prediction. We previously highlighted this by plotting the differences in age-referenced  $v_s$  structure between the Pacific and Atlantic (Figure 1c), showing, for example, that there is a clear average velocity offset. This can be interpreted as the Pacific having a hotter asthenosphere than the Atlantic [cf. Dalton et al., 2014]. Another relative velocity anomaly is localized at ages of  $\sim 80$  Ma, where bathymetry indicates deviations from HSC [e.g., Marty and Cazenave, 1989; Ritzwoller et al., 2004], suggesting thermal resetting by some mechanism [Zhong et al., 2007].

It is likely that some of the thermal boundary layer complexities in isotropic structure discussed above will have a counterpart in anisotropic structure, resulting, e.g., from modified LPO formation. To assess to which extent purely temperature-controlled LPO formation is able to predict anisotropic structure, we visualized (Figure S6) the LPO-based  $\xi$  predictions of Becker et al. [2008] in the same way as the seismic models, referencing them against seafloor age. The LPO models exhibit natural flattening at ages of around 70 Ma, even though no additional mechanisms beyond temperature-controlled LPO have been considered in the underlying geodynamic modeling procedure, presumably because isotropic tomography was used to infer temperature. By fitting the age-dependent model given by equations (5) and (6) through the peak  $\xi$  depths in the LPO model, we can infer slope and flattening parameters ( $c = 2.2$ ,  $f = 66$  Ma for the Pacific, and  $c = 1.9$ ,  $f = 75$  Ma for the Atlantic), which can be directly compared to the seismological results. The flattening parameters turn out to be quite similar to the ones of model B in Figure 2, but the average depth of the zone in the geodynamic LPO model is generally larger (150 km versus 110 km for the Pacific, and 140 km versus 80 km for the Atlantic; Figure S6). While this indicates that flattening itself is not per se an argument against an LPO origin of radial anisotropy, the depth discrepancy provides an additional hint that pure LPO is not an ideal model for radial anisotropy, substantiating the results of Burgos et al. [2014] and Beghein et al. [2014] and contrasting the clear age control that was found for global and regional azimuthal anisotropy [Becker et al., 2014].

### 3.2. Proposed Explanations for Observed Non-HSC-Related Effects

Temperature anomalies, such as the 80 Ma disturbance in the Pacific (Figure 1c), may be associated with an increased asthenospheric partial melt fraction, which has also been suggested as a possible geodynamic-petrological interpretation for the anisotropic structures [Kawakatsu et al., 2009; Schmerr, 2012; Beghein et al., 2014]. Sakamaki et al. [2013] have shown that melt density is highly pressure dependent, causing melt mobility to have a local maximum at depths between 80 and 150 km, coinciding with the range of strong anisotropy (Figure 2). Sakamaki et al. [2013] suggest a tendency for partial melt ponding at the top of the asthenosphere, which, under shear deformation, may be reworked to subhorizontal melt bands [e.g., Holtzman and Kendall, 2010]. The shape-preferred orientation (SPO)-type radial anisotropy due to such melt-related structures may, in turn, be responsible for the impedance contrast observed in receiver functions [Kawakatsu et al., 2009], and high partial melt fractions may also lead to LPO fabrics that are different from the A-type expected for the background asthenosphere [Holtzman et al., 2003; Holtzman and Kendall, 2010]. Ubiquitous partial melt would be consistent with stronger radial anisotropy in the "hot" Pacific compared to the Atlantic (Table S1). However, even the simplified A-type LPO flow models of Becker et al. [2008] indicate stronger radial anisotropy underneath the Pacific, because of more efficient saturation of LPO, cautioning against the interpretation of peak anisotropy strength.

In contrast, Karato [2012, 2014] has argued that the amount of in situ partial melt away from ridges and hot spots probably does not exceed relevant fractions able to cause a significant reduction in  $v_s$  or any of the other observed geophysical anomalies. Instead, Karato [2014, 2015] proposes a mechanism associated with anelastic relaxation based on grain boundary sliding, as an alternative explanation for the MLD and seismic

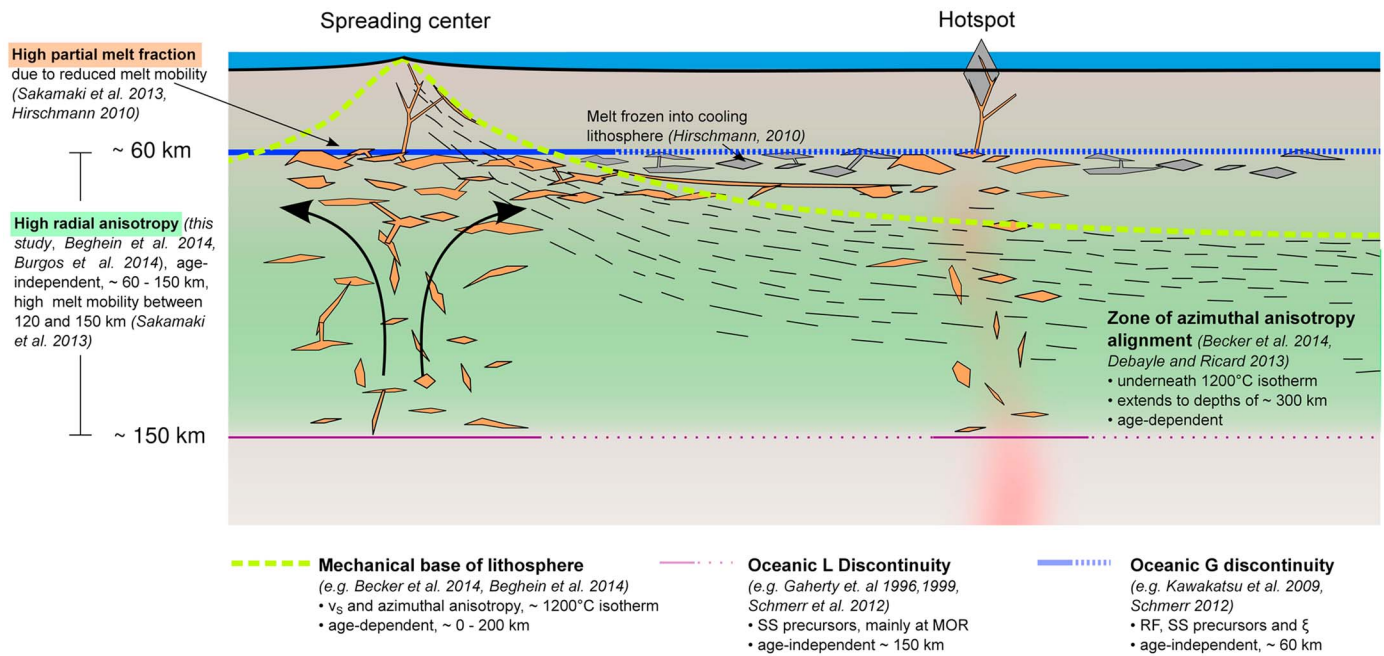


**Figure 4.** Conceptual model of anisotropy and upper mantle seismic discontinuities in the lithosphere-asthenosphere system.

anisotropy at nearly constant depth of 70 km underneath the oceans. On the other hand, while melting itself is expected to focus at mid-ocean ridges and other temperature anomalies, melt-rich structures may interact and freeze into the cooling lithosphere, when pushed away from the ridge.

Recently, the study of  $Po/So$  guided seismic wave arrivals has proven useful to illuminate the amount and characteristics of structures such as possible frozen-in melt-related layering or other forms of petrological fabric alignment at lithospheric depth [Kennett and Furumura, 2013]. Kennett and Furumura [2015] show that pervasive stochastic heterogeneities with horizontal and vertical correlation lengths of ~10 km and ~0.5 km, respectively, provide a good explanation for their  $Po/So$  observations. Since such quasi-laminated petrological fabrics would manifest themselves in the form of radial anisotropy, when seen by longer-period surface waves, Kennett and Furumura [2015] suggest the level of heterogeneity as a potential  $\xi$  proxy.

While our hypothesis tests (Figure 3) confirm that the weak age dependence in tomographically imaged  $\xi$  is not a regularization artifact, the numerous other sources of uncertainties, such as measurement uncertainties or poorly modeled crust, and the small difference in VR between the considered models, underline that future studies need to confirm the observed tendencies.

### 3.3. Unified Conceptual Interpretation

We propose the following model of the oceanic lithosphere (Figure 4): Convective upwelling of mantle material leads to shallow decompression melting and basaltic crust formation underneath the spreading centers [Hirschmann, 2010]. Deeper in the mantle, partial melt accumulates in flow-aligned, melt-rich channels, whose depth range is controlled by melt mobility [Sakamaki et al., 2013] and bracketed by the two SS precursor depth interfaces, mainly observed underneath hot spots and ridges. Melt lamellae are gradually spread out laterally and eventually frozen into the lithosphere at roughly constant depth that is set by the asthenospheric temperature and spreading rate, with some degree of remelting, present at hot spots and other thermal anomalies [Schmerr, 2012]. An SPO type of radial anisotropy results, as suggested by Kawakatsu et al. [2009], which may alternatively be due to petrological fabrics. Flow-induced LPO contributes strongly to these frozen-in structures at asthenospheric depths, again similar to what has been suggested for the continents [Becker et al., 2008]. Frozen-in SPO will have a minor effect on azimuthal anisotropy if there is no preferred anisotropy of lamellae in the horizontal plane; hence, azimuthal anisotropy is mainly sensitive to LPO due to shearing in the uppermost asthenosphere. The region of alignment between flow model predictions and observed azimuthal anisotropy marks the base of the mechanical lithosphere [Debayle and Ricard, 2013; Becker et al., 2014].

#### 4. Conclusions

Our experiments show that seismological-geodynamic hypotheses including a radially anisotropic layer with a strong age dependence achieve lower data fits than models which are weakly age dependent. We infer that the observation of a radially anisotropic layer that is bracketed by two impedance contrasts is a robust feature and could be explained by a combination of mantle flow-induced LPO and partial melting or petrological-fabric-related SPO. While these interfaces provide information about the conditions under which oceanic plates are created, and perhaps remelted, the top interface, *G*, lies within the thermomechanically defined plate and is not a major dynamic control.

#### Acknowledgments

We thank Domenico Giardini, John Herrlund, and Marc Hirschmann for discussions; Andreas Fichtner for providing computational resources via the Swiss National Supercomputing Centre (CSCS), and two anonymous reviewers for their useful comments. T.W.B. thanks E.R.I. and Hitoshi Kawakatsu from the University of Tokyo for hosting him during a sabbatical where this work was initiated in 2011. Our work was supported by the Swiss National Fond (SNF) under grant 2-77808-13 and NSF grants 1417993 and 1361325. Some of the figures have been prepared with GMT [Wessel and Smith, 1991]; the data sets and codes required to reproduce our work are available upon request.

#### References

- Auer, L., L. Boschi, T. W. Becker, T. Nissen-Meyer, and D. Giardini (2014), Savani: A variable-resolution whole-mantle model of anisotropic shear-velocity variations based on multiple datasets, *J. Geophys. Res. Solid Earth*, *119*, 3006–3034, doi:10.1002/2013JB010773.
- Bassin, C., G. Laske, and G. Masters (2000), The current limits of resolution for surface wave tomography in North America, *Eos Trans. AGU*, *81*(48), Fall Meet. Suppl., Abstract F897.
- Becker, T. W., S. Chevrot, V. Schulte-Pelkum, and D. K. Blackman (2006), Statistical properties of seismic anisotropy predicted by upper mantle geodynamic models, *J. Geophys. Res.*, *111*, B08309, doi:10.1029/2005JB004095.
- Becker, T. W., B. Kustowski, and G. Ekström (2008), Radial seismic anisotropy as a constraint for upper mantle rheology, *Earth Planet. Sci. Lett.*, *267*, 213–237, doi:10.1016/j.epsl.2007.11.038.
- Becker, T. W., C. P. Conrad, A. Schaeffer, and S. Lebedev (2014), Origin of azimuthal seismic anisotropy in oceanic plates and mantle, *Earth Planet. Sci. Lett.*, *402*, 236–250, doi:10.1016/j.epsl.2014.06.014.
- Beghein, C., K. Yuan, N. Schmerr, and Z. Xing (2014), Changes in seismic anisotropy shed light on the nature of the Gutenberg discontinuity, *Science*, *343*, 1237–1240, doi:10.1126/science.1246724.
- Boschi, L., and G. Ekström (2002), New images of the Earth's upper mantle from measurements of surface-wave phase velocity anomalies, *J. Geophys. Res.*, *107*(B4), ESE 1–1–ESE 1-14, doi:10.1029/2000JB000059.
- Burgos, G., J.-P. Montagner, E. Beucler, Y. Capdeville, A. Mocquet, and M. Drilleau (2014), Oceanic lithosphere/asthenosphere boundary from surface wave dispersion data, *J. Geophys. Res. Solid Earth*, *119*, 1079–1093, doi:10.1002/2013JB010528.
- Chen, K., and P. Molnar (1983), Focal depths of intracontinental and intraplate earthquakes and their implications for the thermal and mechanical properties of the lithosphere, *J. Geophys. Res.*, *88*, 4183–4214.
- Dalton, C. A., C. H. Langmuir, and A. Gale (2014), Geophysical and geochemical evidence for deep temperature variations beneath mid-ocean ridges, *Science*, *344*, 80–83, doi:10.1126/science.1249466.
- Debayle, E., and Y. Ricard (2013), Seismic observations of large-scale deformation at the bottom of fast-moving plates, *Earth Planet. Sci. Lett.*, *376*, 165–177.
- Dziewoński, A. M., and D. L. Anderson (1981), Preliminary reference Earth model, *Phys. Earth Planet. Inter.*, *25*, 297–356.
- Ekström, G. (2011), A global model of Love and Rayleigh surface wave dispersion and anisotropy, 25–250 s, *Geophys. J. Int.*, *187*, 1668–1686.
- Ekström, G., and A. M. Dziewoński (1998), The unique anisotropy of the Pacific upper mantle, *Nature*, *394*, 168–172, doi:10.1038/28148.
- Ferreira, A. M., J. H. Woodhouse, K. Visser, and J. Trampert (2010), On the robustness of global radially anisotropic surface wave tomography, *J. Geophys. Res.*, *115*, B04313, doi:10.1029/2009JB006716.
- French, S., V. Lekić, and B. Romanowicz (2013), Waveform tomography reveals channelled flow at the base of the oceanic asthenosphere, *Science*, *342*, 227–230, doi:10.1126/science.1241514.
- Gaherty, J. B., T. H. Jordan, and L. S. Gee (1996), Seismic structure of the upper mantle in a central Pacific corridor, *J. Geophys. Res.*, *101*, 22,291–22,310, doi:10.1029/96JB01882.
- Gaherty, J. B., M. Kato, and T. H. Jordan (1999), Seismological structure of the upper mantle: A regional comparison of seismic layering, *Phys. Earth Planet. Inter.*, *110*, 21–41, doi:10.1016/S0031-9201(98)00132-0.
- Gutenberg, B. (1926), Untersuchungen zur Frage, bis zu welcher Tiefe die Erde kristallin ist, *Z. Geophys.*, *2*, 24–29.
- Hansen, L. N., M. E. Zimmerman, and D. L. Kohlstedt (2014), Protracted fabric evolution in olivine: Implications for the relationship among strain, crystallographic fabric, and seismic anisotropy, *Earth Planet. Sci. Lett.*, *387*, 157–168, doi:10.1016/j.epsl.2013.11.009.
- Hirschmann, M. H. (2010), Partial melt in the oceanic low velocity zone, *Phys. Earth Planet. Inter.*, *179*, 60–71, doi:10.1016/j.pepi.2009.12.003.
- Holtzman, B. K., and J. Kendall (2010), Organized melt, seismic anisotropy, and plate boundary lubrication, *Geochem. Geophys. Geosyst.*, *11*, Q0AB06, doi:10.1029/2010GC003296.
- Holtzman, B. K., D. L. Kohlstedt, M. E. Zimmerman, F. Heidelbach, T. Hiraga, and J. Hustoft (2003), Melt segregation and strain partitioning: Implications for seismic anisotropy and mantle flow, *Science*, *301*, 1227–1230.
- Karato, S.-I. (2012), On the origin of the asthenosphere, *Earth Planet. Sci. Lett.*, *321–322*, 95–103, doi:10.1016/j.epsl.2012.01.001.
- Karato, S.-I. (2014), Does partial melting explain geophysical anomalies?, *Phys. Earth Planet. Inter.*, *228*, 300–306, doi:10.1016/j.pepi.2013.08.006.
- Karato, S.-I. (2015), Mechanisms and geologic significance of the mid-lithosphere discontinuity in the continents, *Nat. Geosci.*, *8*, 509–514, doi:10.1038/NGEO2462.
- Karato, S.-I., H. Jung, I. Katayama, and P. Skemer (2008), Geodynamic significance of seismic anisotropy of the upper mantle: New insights from laboratory studies, *Annu. Rev. Earth Planet. Sci.*, *36*, 59–95, doi:10.1146/annurev.earth.36.031207.124120.
- Kawakatsu, H., P. Kumar, Y. Takei, M. Shinohara, T. Kanazawa, E. Araki, and K. Suyehiro (2009), Seismic evidence for sharp lithosphere-asthenosphere boundaries of oceanic plates, *Science*, *324*, 499–502, doi:10.1126/science.1169499.
- Kennett, B. L. N., and T. Furumura (2013), High-frequency *Po/So* guided waves in the oceanic lithosphere: I – long-distance propagation, *Geophys. J. Int.*, *195*, 1862–1877, doi:10.1093/gji/ggt344.
- Kennett, B. L. N., and T. Furumura (2015), Towards the reconciliation of seismological and petrological perspectives on oceanic lithosphere heterogeneity, *Geochem. Geophys. Geosyst.*, *16*, 3129–3141, doi:10.1002/2015GC006017.
- Kumar, P., and H. Kawakatsu (2011), Imaging the seismic lithosphere-asthenosphere boundary of the oceanic plate, *Geochem. Geophys. Geosyst.*, *12*, Q01006, doi:10.1029/2010GC003358.
- Kustowski, B., G. Ekström, and A. M. Dziewoński (2008), Anisotropic shear-wave velocity structure of the Earth's mantle: A global model, *J. Geophys. Res.*, *113*, B06306, doi:10.1029/2007JB005169.

- Laske, G., G. Masters, Z. Ma, and M. Pasyanos (2013), Update on CRUST1.0—A 1-degree global model of Earth's crust, Geophysical Research Abstracts Vol. 15, EGU2013-2658 presented at EGU General Assembly 2013, held 7–12 April, 2013 in Vienna, Austria.
- Long, M. D., and T. W. Becker (2010), Mantle dynamics and seismic anisotropy, *Earth Planet. Sci. Lett.*, *297*, 341–354, doi:10.1016/j.epsl.2010.06.036.
- Maggi, A., E. Debayle, K. Priestley, and G. Barruol (2006), Azimuthal anisotropy of the Pacific region, *Earth Planet. Sci. Lett.*, *250*, 53–71.
- Marty, J. C., and A. Cazenave (1989), Regional variations in subsidence rate of oceanic plates: A global analysis, *Earth Planet. Sci. Lett.*, *94*, 301–315.
- McKenzie, D., J. Jackson, and K. Priestley (2005), Thermal structure of oceanic and continental lithosphere, *Earth Planet. Sci. Lett.*, *233*, 337–349, doi:10.1016/j.epsl.2005.02.005.
- Montagner, J.-P., and T. Tanimoto (1991), Global upper mantle tomography of seismic velocities and anisotropies, *J. Geophys. Res.*, *96*, 20,337–20,351.
- Moulik, P., and G. Ekström (2014), An anisotropic shear velocity model of the Earth's mantle using normal modes, body waves, surface waves and long-period waveforms, *Geophys. J. Int.*, *199*(3), 1713–1738, doi:10.1093/gji/ggu356.
- Müller, R. D., M. Sdrolias, C. Gaina, and W. R. Roest (2008), Age, spreading rates and spreading asymmetry of the world's ocean crust, *Geochem. Geophys. Geosyst.*, *9*, Q04006, doi:10.1029/2007GC001743.
- Nettles, M., and A. M. Dziewoński (2008), Radially anisotropic shear-velocity structure of the upper mantle globally and beneath North America, *J. Geophys. Res.*, *113*, B02303, doi:10.1029/2006JB004819.
- Plomerová, J., D. Kouba, and V. Babuška (2002), Mapping the lithosphere-asthenosphere boundary through changes in surface-wave anisotropy, *Tectonophysics*, *58*, 175–185.
- Priestley, K., and D. McKenzie (2013), The relationship between shear wave velocity, temperature, attenuation and viscosity in the shallow part of the mantle, *Earth Planet. Sci. Lett.*, *381*, 78–91.
- Revenaugh, J., and T. H. Jordan (1991), Mantle layering from ScS reverberations: 3. The upper mantle, *J. Geophys. Res.*, *96*, 19,781–19,810.
- Ritzwoller, M. H., N. M. Shapiro, and S. Zhong (2004), Cooling history of the Pacific lithosphere, *Earth Planet. Sci. Lett.*, *226*, 69–84, doi:10.1016/j.epsl.2004.07.032.
- Rychert, C. A., and P. M. Shearer (2009), A global view of the lithosphere-asthenosphere boundary, *Science*, *324*, 495–498.
- Rychert, C. A., and P. M. Shearer (2011), Imaging the lithosphere-asthenosphere boundary beneath the Pacific using SS waveform modeling, *J. Geophys. Res.*, *116*, B07307, doi:10.1029/2010JB008070.
- Rychert, C. A., N. Schmerr, and N. Harmon (2012), The Pacific lithosphere-asthenosphere boundary: Seismic imaging and anisotropic constraints from SS waveforms, *Geochem. Geophys. Geosyst.*, *13*, Q0AK10, doi:10.1029/2012GC004194.
- Sakamaki, T., A. Suzuki, E. Ohtani, H. Terasaki, S. Urakawa, Y. Katayama, K.-I. Funakoshi, Y. Wang, J. W. Hearn, and M. D. Ballmer (2013), Ponded melt at the boundary between the lithosphere and asthenosphere, *Nat. Geosci.*, *6*, 1041–1044, doi:10.1038/NGEO1982.
- Schmerr, N. (2012), The Gutenberg discontinuity: Melt at the lithosphere-asthenosphere boundary, *Science*, *335*, 1480–1483, doi:10.1126/science.1215433.
- Selway, K., H. Ford, and P. Keleman (2015), The seismic mid-lithosphere discontinuity, *Earth Planet. Sci. Lett.*, *414*, 45–57, doi:10.1016/j.epsl.2014.12.029.
- Tarantola, A. (2006), Popper, Bayes and the inverse problem, *Nat. Phys.*, *2*, 492–494.
- Turcotte, D. L., and G. Schubert (2002), *Geodynamics*, 2nd ed., Cambridge Univ. Press, Cambridge, U. K.
- Visser, K., J. Trampert, and B. L. N. Kennett (2008), Global anisotropic phase velocity maps for higher mode Love and Rayleigh waves, *Geophys. J. Int.*, *172*, 1016–1032.
- Watts, A. B., J. Hunter, and S. S. J. Zhong (2013), The behavior of the lithosphere on seismic to geologic timescales, *Annu. Rev. Earth Planet. Sci.*, *41*, 443–468, doi:10.1146/annurev-earth-042711-105457.
- Wessel, P., and W. H. F. Smith (1991), Free software helps map and display data, *Eos Trans. AGU*, *72*, 441–446, doi:10.1029/90EO00319.
- Zhang, Y. S., and T. Tanimoto (1991), Global Love wave phase velocity variation and its significance to plate tectonics, *Phys. Earth Planet. Inter.*, *66*, 160–202, doi:10.1016/0031-9201(91)90075-S.
- Zhong, S., M. Ritzwoller, N. Shapiro, W. Landuyt, J. Huang, and P. Wessel (2007), Bathymetry of the Pacific plate and its implications for thermal evolution of lithosphere and mantle dynamics, *J. Geophys. Res.*, *112*, B06412, doi:10.1029/2006JB004628.